# Effective media models for wave propagation in prestressed fractured rocks with nonlinear elastic and hyperelastic deformations

Li-Yun Fu*[1,2], Haidi Yang[1,2], Bo-Ye Fu[3], and Tobias M. Müller[1,2]

[1]*National Key Laboratory of Deep Oil and Gas, China University of Petroleum (East China), Qingdao, 266580, P. R. China*
[2]*Laboratory for Marine Mineral Resources, Laoshan Laboratory, Qingdao 266071, P. R. China*
[3]*Beijing University of Technology, Beijing, 100124, China*
** Corresponding author: lfu@upc.edu.cn (L.-Y. Fu)*

## ABSTRACT

Stress-induced progressive deformations in fractured rocks with increasing effective pressure generally undergo nonlinear elastic (due to the closure of compliant pores), hyperelastic (due to residual stress), and inelastic (due to fracture growth) deformations prior to mechanical failure. Wave propagation in such rocks involves the complex interaction of fracture- and stress-induced changes in both velocity and anisotropy. With attention to nonlinear elastic and hyperelastic deformations, we incorporate acoustoelasticity into the traditional Hudson/Cheng models to describe the coupling of fracture-induced and stress-induced anisotropies. The resulting acoustoelastic Hudson model (AHM) is valid for the crack density smaller than 0.1 whereas the Padé AHM could handle higher crack densities. We extend the Padé AHM to consider the stress-induced crack closure with nonlinear elastic deformations by incorporating the dual-porosity model. These models approach the coupled anisotropies with different accuracies and computational complexities. The plane-wave analyses and effective-moduli calculations of stressed fractured rocks with varying crack densities determine the accuracy of these models under the isotropic (confining) and anisotropic (uniaxial and pure shear) prestress conditions. The relevant Thomsen parameters are applied to experimental data to validate the applicability. Finite-difference simulations are implemented to identify the contribution of different anisotropies through the variety of wavefronts, depending on fracture orientation, crack density, prestress mode and magnitude, and loading direction. Particular attention is paid to the anisotropic prestress, where the coupled anisotropies are constructive or destructive interference, strongly related to the relativity between fracture strike and loading direction. The stress-induced crack closure will reduce the fracture anisotropy so that the stress-induced background anisotropy dominates the shape of wavefronts with increasing prestress.

**Keywords:** Stressed fractured rocks, Wave propagation, Acoustoelastic Hudson/Cheng models, Coupled anisotropies, Crack closure

## 1. Introduction

The presence of fractures in crustal rocks is often associated with tectonic stress, overburden pressure, and geopressure. The nonlinear stress dependence of elastic properties is strongly related to finite deformations in compliant pores under large-magnitude pressure (Adams and Williamson, 1923; Walsh, 1965; Nur and Simmons, 1969; Cheng and Toksöz, 1979). Wave propagation in fractured rocks is always sensitive to external pressure due to the stress-induced anisotropy and closure of fractures. For this reason, seismic data can be employed to detect fractures and interpret in-situ stress/geopressure fields. However, seismic anisotropy in prestressed fractured rocks involves an extremely complex coupling process of fracture-induced anisotropy and stress-induced background anisotropy, both changing reciprocally with increasing pressure. Despite the large scaling difference between fracture size and wavelength, numerous studies have dealt with the seismic anisotropy of fractured rocks (e.g., Helbig and Thomsen, 2005; Grechka and Kachanov, 2006), but mostly in the framework of the effective elasticity of fractured rocks without regard to the effect of external pressure. The coupling process of fracture- and stress-induced anisotropies remains largely unaddressed theoretically for fractured rocks. In this study, we intend to fill this gap by incorporating acoustoelasticity into Hudson's (1980, 1981) and Cheng's (1993) effective media theories. It is worth mentioning that a similar work to Cheng (1993) is proposed by Nizizawa (1982) in which a differential embedding scheme was applied to the Eshelby theory (Eshelby, 1957) to model higher crack densities with a transversely isotropic background.

Acoustoelasticity extends the classical theory of elasticity to stress-induced hyperelasticity in isotropic solids with residual stress (e.g., Thurston and Brugger, 1964; Norris, 1983) by merging a cubic term into the

strain energy function. The associated elastic moduli are known as the third-order elastic constants (3oeCs) (Green, 1973). The stress-induced anisotropy of effective elastic moduli is of orthotropic feature (e.g., Pao and Gamer, 1985) strongly related to the orientation of prestresses. The theory has been employed to explain stress-induced elastic modulus variations in rocks (e.g., Johnson and Shankland, 1989; Meegan et al., 1993; Johnson & Rasolofosaon, 1996), providing an alternative method to understand the stress-induced azimuthal anisotropies in ultrasonic velocity (Sayers, 1988) and in borehole flexural waves (Sinha and Kostek, 1996). Therefore, the acoustoelastic method has been applied to well-logging data for the remote monitoring of in-situ stresses (e.g., Cao et al., 2004; Lei et al., 2012). The conventional acoustoelasticity in solids has been extended to porous media by incorporating Biot's theory, known as acoustoporoelasticity (e.g., Grinfeld and Norris, 1996; Ba et al., 2013). Great progress has been made in acoustoelastic FD simulations of wave propagation in stressed solids (Liu and Sinha, 2000; Chen et al., 2006; Yang et al., 2022a) for further insights into the stress-induced anisotropy in wavefields. FD numerical simulations are extended to acoustoporoelastic equations for wave propagation in prestressed porous rocks under the isotropic and anisotropic prestress conditions (Yang et al., 2022b).

The acoustoelastic 3oeCs of rocks are usually measured by a linear fit of experimental data of elastic moduli versus pressures (Winkler and Liu, 1996; Winkler and McGowan, 2004; Wang and Schmitt, 2021). However, numerous experiments with porous/fractured rocks demonstrate a nonlinear relation between them due to the closure of compliant pores. Prioul et al. (2004) use different sets of 3oeCs to fit the stress-dependent elastic moduli of the same rock sample in different ranges of stresses. Ba et al. (2013) compare experimental measurements under the "jacketed" and the "unjacketed" conditions, showing the important influence of crack deformations on the 3oeCs. Sripanich et al. (2021) further study the connection between the 3oeCs and microstructures for stress-dependent wave propagation. Strictly speaking, the acoustoelastic 3oeCs are only applicable to linear strains (via displacements) (Sinha and Plona, 2001). In this sense, the acoustoelastic deformation should refer to the linear segment in the stress-strain curve. It follows an initial nonlinear segment caused by the closure of compliant pores during the loading process, which accumulates the residual stress inside porous/fractured rocks.

The acoustoelastic 3oeCs are strictly valid for an isotropic homogeneous medium. The extension to fractured rocks has become a rapidly growing area of research, particularly focusing on the stress-induced elastic nonlinearity due to the closure of compliant structures. A weak-anisotropy approximation (Bakulin et al., 2000; Sarkar et al., 2003) is formulated by considering the stress-induced change of the isotropic background into an orthorhombic solid, whereas the fracture-induced anisotropy remains unchanged, which, however, seems impossible because long, narrow cracks (low aspect ratio) close at relatively low pressures. Taylor expansion is not an accurate method to approximate the energy function of large strains, whereas Padé approximation features well-posed at low-order terms because of its mathematical properties (Trefethen and Halpern, 1986). Replacing the Taylor expansion used in the derivation of classical acoustoelastic 3oeCs, the Padé expansion is used to approximate the strain energy function for large-amplitude strains (Fu and Fu, 2017; Zheng et al., 2024). The resulting Padé acoustoelastic 3oeCs can account for strong elastic nonlinearity under large prestresses. However, these works, like the conventional acoustoelastic 3oeCs, are formulated from the strain energy function of isotropic rocks by ignoring microstructures, and thus only provide a model-independent description of stress-dependent elastic moduli for fractured rocks. The dual-porosity model (Shapiro, 2003) has been incorporated into the conventional acoustoelastic 2oeCs (Fu and Fu, 2018) and 3oeCs (Fu et al., 2020) for describing the stress dependency of compliant pores. Ling et al. (2021) incorporate the David-Zimmerman model (David and Zimmerman, 2012) to improve the accuracy of acoustoelasticity by considering the stress-induced closure of cracks. Wei et al. (2022) investigate the squirt-flow effect on the stress-dependent elastic moduli. An acoustoelastic Mori-Tanaka (MT) model is formulated for the effective 3oeCs of stressed fractured rocks (Fu et al., 2023a), This analytical model is extended to account for the closure of cracks (Fu et al., 2023b) by incorporating the David-Zimmerman model. These aforementioned studies focus on the acoustoelastic 3oeCs extended to fractured rocks, but are lacking an efficient and simplified way to couple the stress-induced background anisotropy and fracture-induced anisotropy of fractured rocks.

Wave propagation in stressed fractured rocks generates fracture- and stress-induced anisotropies (Rasolofosaon, 1998; Jaeger et al., 2007). The former refers to that caused by bedding, directed microcracks, or aligned fractures, and therefore is influenced by the closure of compliant pores (Sayers, 2002) with increasing pressure. The latter usually includes the stress-induced velocity anisotropy in the isotropic background. The coupling of these two anisotropies involves complicated interactions to be addressed particularly under the anisotropic prestress. Even for a uniform confining pressure, the resulting strains present an anisotropic distribution depending on the preferred orientation of aligned fractures. The commonly used Hudson's anisotropic model (Hudson, 1981) is a simple and practical model for fracture-

induced anisotropies though with a limited accuracy inferior to many other theories. It is based on a scattering-theory analysis of the mean wavefield in an elastic solid with thin, penny-shaped ellipsoidal cracks. The unphysical behavior associated with the Hudson's second-order formula can be avoided by the Padé expansion (Cheng, 1993). Applications to fractured coals demonstrate that the Cheng's anisotropic model can handle higher crack densities (Shuck et al., 1996; Pei et al., 2012). In this study, we incorporate the acoustoelastic 3oeCs into the Hudson/Cheng models to introduce crack density for describing the stress-dependent anisotropies of fractured rocks under different pressure conditions. It should be stressed that both the effective models tremendously simplify real fractured rocks by many assumptions and limitations (see Mavko et al., 2009). They are actually a phenomenological model by ignoring specific microstructures, and only provide a model-independent description of effective anisotropic properties of aligned cracks. What we concern is whether the stress-induced changes imposed on cracks violate the assumptions and limitations. We will address this issue in relative chapters and make a comprehensive discussion.

We first briefly introduce the Hudson/Cheng models and acoustoelasticity by focusing on the stiffness matrices under different prestress conditions. We then formulate the acoustoelastic Hudson/Cheng models through the displacement of stiffness matrices. We extend these models to account for the stress-induced closure cracks by incorporating the dual-porosity model (Shapiro, 2003). Plane-wave analyses are then conducted to compare phase velocities of these acoustoelastic Hudson models and their effective moduli of stressed fractured rocks with varying crack densities. The effective Thomsen parameters are formulated to describe the coupling of fracture- and stress-induced anisotropies of stressed fractured rocks. Applications to experimental data with fractured rocks differentiate these acoustoelastic models in accuracy with comparison to the weak-anisotropy model (Sarkar et al., 2003; Prioul et al., 2004). Finally, based on the stiffness matrix of these acoustoelastic models, we conduct acoustoelastic finite-difference numerical simulations for stress-dependent wave propagation in stressed fractured media.

## 2. Theory

The theory of acoustoelastic 3oeCs is derived from crystals. It has much success in solid materials (e.g., metal). Applications to fractured rocks are based on a general description that ignores microcracks, and therefore show large errors (e.g., Winkler and McGowan, 2004; Fu and Fu, 2018; Fu et al., 2020) because of the involvement of fracture-induced anisotropy and stress-induced closure of cracks. The Hudson model (Hudson, 1980) has been widely used to describe anisotropic fractured rocks with small (Hudson, 1981) and large (Cheng, 1993) crack densities. We follow the Hudson method to extend classical acoustoelastic 3oeCs to fractured rocks under the prestress. We incorporate the dual-porosity model (Shapiro, 2003) to account for the stress-induced closure of cracks. The parameterization model used in this study to compute effective stiffness tensors composes of a group of aligned fractures that are embedded into an isotropic background medium subject to different prestress conditions (confining, uniaxial, and pure-shear).

### 2.1. Classical acoustoelastic model

Compared to the linear elastic theory (2oeCs) with two elastic constants (Lamé constants $\lambda$ and $\mu$) for an isotropic medium, the third-order elasticity (3oeCs) invokes three additional elastic constants (sometimes called $A$, $B$, and $C$) (Green, 1973; Pao and Gamer, 1985). The detailed equations can be referred to Yang et al. (2022a). We apply the theory to the isotropic background of stressed fractured rocks. For convenience, we assume the values of indices $i$ and $j$ (the Voigt abbreviated symbols) as 1 and 3, indicating the coordinates $x$ and $z$ for the 2D case. The acoustoelastic stiffness matrix $\mathbf{A}^{(0)}$ for the stressed background can be represented as

$$\mathbf{A}^{(0)} = \begin{bmatrix} A_{11}^{(0)} & A_{13}^{(0)} & 0 \\ A_{31}^{(0)} & A_{33}^{(0)} & 0 \\ 0 & 0 & A_{55}^{(0)} \end{bmatrix}. \tag{1}$$

Based on the definition of Goldberg (1961), the 20 third-order constants due to the symmetry for the 2D case can be reduced to three constants (e.g., $A$, $B$, and $C$) for an isotropic medium subject to prestress loading. Therefore, the effective acoustoelastic constants $A_{ij}^{(0)}$ can be reduced to

$$\begin{cases} A_{11}^{(0)} = (\lambda + 2\mu)(1 + 3e_{11} - e_{33}) + (6B + 2C + 2A)e_{11} + (2B + 2C)e_{33} \\ A_{13}^{(0)} = \lambda(1 + e_{11} + e_{33}) + (2B + 2C)(e_{11} + e_{33}) \\ A_{33}^{(0)} = (\lambda + 2\mu)(1 - e_{11} + 3e_{33}) + (6B + 2C + 2A)e_{33} + (2B + 2C)e_{11} \\ A_{55}^{(0)} = \mu(1 + e_{11} + e_{33}) + \left(B + \frac{A}{2}\right)(e_{11} + e_{33}) \end{cases}, \tag{2}$$

where $e_{ij}$ are the elements of the total prestrain tensor. The prestrain $e_{ij}$ in the classical acoustoelasticity are approached as a linear function of displacements under the small disturbance assumption (Pao and Gamer, 1985).

For the specific loading modes (confining, uniaxial, and pure-shear), the resulting tensors have the same null components as that for transversely isotropic (TI) media with the symmetry axis aligned with one of the coordinate directions, and therefore $A_{ij}^{(0)}$ can be simplified. For the isotropic case with the hydrostatic confining pressure $P$, the principal strain components are written as

$$\begin{cases} e_{11} = e_{33} = -\frac{P}{3K}, \\ e_{13}=0, \end{cases} \quad (3)$$

where $K$ is the bulk modulus. For the uniaxial pressure $P$, the stress field is anisotropic with the symmetry axis aligned with the direction of $P$. The compressed axis is shortened and the other is elongated, both having different strains. These principal strain components are expressed as

$$\begin{cases} e_{11} = \frac{P}{E} = \frac{P(\lambda+\mu)}{\mu(3\lambda+2\mu)}, \\ e_{33} = -\frac{\nu}{E} = -\frac{P\lambda}{2\mu(3\lambda+2\mu)}, \\ e_{13}= 0, \end{cases} \quad (4)$$

where $E$ and $\nu$ are Young's modulus and Poisson's ratio, respectively. For the pure-shear pressure $P$, both the compressed and elongated axes have the same absolute value of strains. These principal strain components become

$$\begin{cases} e_{11} = -e_{33} = \frac{P}{2\mu}, \\ e_{13} = 0. \end{cases} \quad (5)$$

Substituting equations (3)-(5) into (2), respectively, yields the corresponding acoustoelastic stiffness matrices of these three loading modes, with their deformation progressions detailed in Yang et al. (2022a).

## 2.2. Conventional Hudson/Cheng models

The conventional Hudson second-order expansion of the effective stiffness constants $C_{ij}$ for small aspect-ratio ellipsoidal cracks free of pressures are given as (Hudson, 1981)

$$C_{ij} = C_{ij}^{(0)} + C_{ij}^{(1)} + C_{ij}^{(2)}, \quad (6)$$

where $C_{ij}^{(0)}$ are the isotropic background moduli and $C_{ij}^{(1)}$ and $C_{ij}^{(2)}$ are the first- and second-order perturbations, respectively, for one set of aligned cracks with their normal along the symmetry axis. These matrix elements are given by

$$\begin{cases} C_{11}^{(0)} = C_{33}^{(0)} = \lambda + 2\mu \\ C_{13}^{(0)} = \lambda \\ C_{55}^{(0)} = \mu \end{cases}, \quad \begin{cases} C_{11}^{(1)} = -\frac{\lambda^2}{\mu}\epsilon U_3 \\ C_{13}^{(1)} = -\frac{\lambda(\lambda+2\mu)}{\mu}\epsilon U_3 \\ C_{33}^{(1)} = -\frac{(\lambda+2\mu)^2}{\mu}\epsilon U_3 \\ C_{55}^{(1)} = -\mu\epsilon U_1 \end{cases},$$

$$\text{and} \quad \begin{cases} C_{11}^{(2)} = \frac{q}{15}\frac{\lambda^2}{\lambda+2\mu}(\epsilon U_3)^2 \\ C_{13}^{(2)} = \frac{q}{15}\lambda(\epsilon U_3)^2 \\ C_{33}^{(2)} = \frac{q}{15}(\lambda+2\mu)(\epsilon U_3)^2 \\ C_{55}^{(2)} = \frac{q}{15}\frac{\mu(3\lambda+8\mu)}{\lambda+2\mu}(\epsilon U_1)^2 \end{cases}, \quad (7)$$

where $\epsilon$ is the crack density, $U_1$ and $U_3$ are to be defined for various inclusions, and $q = 15\frac{\lambda^2}{\mu^2} + 15\frac{\lambda}{\mu} + 28$ (Hudson, 1981).

The Hudson model (HM) is derived based on a scattering-theory analysis of the mean wavefield in an elastic solid with thin, penny-shaped ellipsoidal cracks, with several assumptions and limitations applied (Mavko et al., 2009). The crack radius and the distance between cracks are much smaller than a wavelength. The model is appropriate for high-frequency laboratory conditions, but with cracks isolated with respect to fluid flow. The formal limit of the model is $\epsilon$ less than 0.1. The second-order expansion becomes unphysical beyond the formal limit, which can be avoided by the Padé expansion (Cheng, 1993). The resulting Padé Hudson model (Padé HM) can be expressed as

$$C_{ij} = C_{ij}^{(0)}\frac{1-a_{ij}\epsilon}{1+b_{ij}\epsilon}, \quad (8)$$

with the Padé coefficients,

$$\begin{cases} a_{ij} = -C_{ij}^{(1)}/C_{ij}^{(0)}\epsilon - b_{ij} \\ b_{ij} = -C_{ij}^{(2)}/C_{ij}^{(1)}\epsilon \end{cases}. \quad (9)$$

The Padé HM also follows the assumptions and limitations applied to the Hudson model except that it can handle arbitrary aspect ratios (Mavko et al., 2009), unlike the Hudson model that assumes very small aspect ratio ellipsoidal cracks. Both the HM and Padé HM are the phenomenological models for effective anisotropic properties of aligned cracks with a spatially homogeneous distribution. We will discuss the stress-induced changes imposed on cracks subsequently, which may affect these assumptions and limitations.

## 2.3. Acoustoelastic Hudson/Cheng models

Based on the Hudson/Cheng models, higher orders with the expansion from the background acoustoelastic constants should account for the effective stiffness of stressed fractures. The fracture-induced anisotropy is modulated by prestresses and is superimposed on the stress-induced background anisotropy.

Under the same assumption of small-aspect-ratio, penny-shaped ellipsoidal cracks, the acoustoelastic Hudson model (AHM) can be expressed as

$$A_{ij} = A_{ij}^{(0)} + A_{ij}^{(1)} + A_{ij}^{(2)}, \quad (10)$$

where $A_{ij}$ denotes the effective acoustoelastic constants for stressed fractured rocks, $A_{ij}^{(0)}$ is the background acoustoelastic constants, and $A_{ij}^{(1)}$ and $A_{ij}^{(2)}$ are the first- and second-order disturbations for aligned fractures, respectively. Similarly, these matrix elements are given by

$$\begin{cases} A_{11}^{(1)} = -\frac{(A_{13}^{(0)})^2}{A_{55}^{(0)}}\epsilon U_3' \\ A_{13}^{(1)} = -\frac{A_{13}^{(0)}A_{11}^{(0)}}{A_{55}^{(0)}}\epsilon U_3' \\ A_{33}^{(1)} = -\frac{2\,A_{11}^{(0)}}{A_{55}^{(0)}}\epsilon U_3' \\ A_{55}^{(1)} = -A_{55}^{(0)}\epsilon U_1' \end{cases}, \quad \text{and} \quad \begin{cases} A_{11}^{(2)} = \frac{q'}{15}\frac{(A_{13}^{(0)})^2}{A_{11}^{(0)}}(\epsilon U_3')^2 \\ A_{13}^{(2)} = \frac{q'}{15}A_{13}^{(0)}(\epsilon U_3')^2 \\ A_{33}^{(2)} = \frac{q'}{15}A_{11}^{(0)}(\epsilon U_3')^2 \\ A_{55}^{(2)} = \frac{2}{15}\frac{A_{55}^{(0)}(3A_{13}^{(0)}+8A_{55}^{(0)})}{A_{11}^{(0)}}(\epsilon U_1')^2 \end{cases}, \quad (11)$$

where $q' = 5\frac{(A_{13}^{(0)})^2}{(A_{55}^{(0)})^2} + 15\frac{A_{13}^{(0)}}{A_{55}^{(0)}} + 28$, and $U_1'$ and $U_3'$

are defined for various inclusions under different prestresses. For dry cracks, $U_1' = \frac{16A_{11}^{(0)}}{3\left(3A_{13}^{(0)}+4A_{55}^{(0)}\right)}$ and $U_3' = \frac{4A_{11}^{(0)}}{3\left(3A_{13}^{(0)}+4A_{55}^{(0)}\right)}$. For fluid-filled cracks, $U_1' = \frac{16A_{11}^{(0)}}{3\left(3A_{13}^{(0)}+4A_{55}^{(0)}\right)}$ and $U_3' = \frac{4A_{11}^{(0)}}{3\left(A_{13}^{(0)}+A_{55}^{(0)}\right)(1+K')}$ with $K' = \frac{K_f}{\pi\alpha A_{55}^{(0)}A_{11}^{(0)}}$ where $K_f$ and $\alpha$ represent the bulk modulus of fluid and the aspect ratio of ellipsoidal cracks, respectively. It should be stressed that the underlying assumption for equation (10) is the non-closure of stressed fractures.

Likewise, the second-order AHM is valid for small crack densities and becomes unphysical for larger crack densities, which can be avoided by the Padé expansion. The resulting Padé AHM stiffness tensor can be expressed as

$$A_{ij} = A_{ij}^{(0)}\frac{1-\tilde{a}_{ij}\epsilon}{1+\tilde{b}_{ij}\epsilon}, \tag{12}$$

where the Padé coefficients can be obtained by following Cheng (1993) as follows,

$$\begin{cases}\tilde{a}_{ij} = -A_{ij}^{(1)}/A_{ij}^{(0)}\epsilon - \tilde{b}_{ij}\\ \tilde{b}_{ij} = -A_{ij}^{(2)}/A_{ij}^{(1)}\epsilon\end{cases}. \tag{13}$$

It is worth mentioning that both the AHM and Padé AHM assume that there are no stress-induced changes imposed on aligned cracks. However, the stress-induced acoustoelastic effect makes the isotropic background anisotropic.

### 2.4 Padé acoustoelastic Hudson model with the closure of cracks (AHCM)

Both the AHM and Padé AHM extend the acoustoelastic 3oeCs to stressed fractured rocks, accounting for both the fracture- and stress-induced anisotropies, but with the non-closure assumption of stressed fractures. Considering that compliant cracks are very sensitive to external stresses, there should be another scenario of elastic nonlinearity with large deformations due to the closure of compliant cracks even under small external stresses. The dual-porosity model (Shapiro, 2003; Shapiro and Kaselow, 2005) separates the pore space into stiff and compliant parts, with the effective compliance formulated to describe the stress-dependent compliant porosity due to the closure of cracks. Shapiro (2017) extends the empirical model to anisotropic rocks where the principal stresses are not aligned with the symmetrical axes of the unstressed anisotropic material. However, the porosity deformation approach is built in the frame of poroelasticity, and therefore ignores the effect of prestress on the isotropic background. Based on the dual-porosity model, we follow Fu and Fu (2018) to extend the Padé AHM to account for the closure of stressed compliant cracks.

The stress dependence of elastic anisotropy can be explicitly simplified into equations (37)-(53) of Shapiro (2017) if the contribution of stiff pores is neglected. We rewrite these equations as

$$S_{ij} = S_{ij}^{\mathrm{drs}} + S_{ij}^{*}, \tag{14}$$

where $S_{ij}$ is the stress-dependent elastic compliance of fractured rocks and $S_{ij}^{\mathrm{drs}}$ is the drained compliance of the reference rock. $S_{ij}^{*}$ indicates the stress-dependent compliance due to the closure of the compliant pore space, which is expressed as (Shapiro, 2017)

$$S_{ij}^{*} = \begin{bmatrix} F_c\phi_{11}e^{F_c\sigma_1} & 0 & \frac{F_c\phi_{13}e^{\frac{F_c(\sigma_1+\sigma_3)}{2}}}{2}\\ 0 & F_c\phi_{33}e^{F_c\sigma_3} & \frac{F_c\phi_{13}e^{\frac{F_c(\sigma_1+\sigma_3)}{2}}}{2}\\ 0 & 0 & \frac{F_c\left(\phi_{11}e^{F_c\sigma_1}+\phi_{33}e^{F_c\sigma_3}\right)}{4}\end{bmatrix}, \tag{15}$$

where $\phi_{ij}$ denotes such changes that are necessary to open the compliant part of the pore space of the unloaded rock, the applied effective stress tensor $\sigma_i$ denotes the principal components, and $F_c = C^{\mathrm{drs}}\theta^c$ with $C^{\mathrm{drs}}$ as the bulk compressibility of the reference rock and $\theta^c$ as the dimensionless tensors defined by Shapiro (2017).

Inverting the compliance matrix $S_{ij}^{*}$ in equation (15) yields the corresponding stiffness matrix as

$$B_{ij}^{*} = \begin{bmatrix} B_{11}^{*} & 0 & B_{15}^{*}\\ 0 & B_{33}^{*} & B_{35}^{*}\\ 0 & 0 & B_{55}^{*}\end{bmatrix}, \tag{16}$$

where the elements of this matrix are given as

$$\begin{cases} B_{11}^{*} = \frac{1}{F_c\phi_{11}e^{F_c\sigma_1}},\\ B_{15}^{*} = -\frac{2\phi_{13}e^{\frac{F_c(\sigma_1+\sigma_3)}{2}}}{F_c\phi_{11}e^{F_c\sigma_1}\left(\phi_{11}e^{F_c\sigma_1}+\phi_{33}e^{F_c\sigma_3}\right)},\\ B_{33}^{*} = \frac{1}{F_c\phi_{33}e^{F_c\sigma_3}},\\ B_{35}^{*} = \frac{2F_c\phi_{12}\phi_{23}e^{\frac{F_c(\sigma_1+\sigma_2)}{2}}e^{\frac{F_c(\sigma_2+\sigma_3)}{2}} - 2F_c\phi_{13}e^{\frac{F_c(\sigma_1+\sigma_3)}{2}}\left(\phi_{22}e^{F_c\sigma_2}+\phi_{33}e^{F_c\sigma_3}\right)}{F_c^2\phi_{11}e^{F_c\sigma_1}\left(\phi_{11}e^{F_c\sigma_1}+\phi_{33}e^{F_c\sigma_3}\right)\left(\phi_{11}e^{F_c\sigma_1}+\phi_{22}e^{F_c\sigma_2}\right)},\\ B_{55}^{*} = \frac{4}{F_c\left(\phi_{11}e^{F_c\sigma_1}+\phi_{33}e^{F_c\sigma_3}\right)}. \end{cases} \tag{17}$$

For small prestresses or zero-prestress cases, fractures are not closed and $B_{ij}^{*}$ should have a similar estimating precision to the first-order correction $A_{ij}^{(1)}$ in the AHM, both having first-order calculation accuracy. To illustrate this, we consider horizontal fractures associated with a vertical transverse isotropy (VTI). Based on Shapiro (2017), equation (16) reduces to

$$B_{ij}^{*} = \begin{bmatrix} \frac{1}{F_c\phi_{11}e^{F_c\sigma_1}} & 0 & 0\\ 0 & 0 & 0\\ 0 & 0 & \frac{4}{F_c\phi_{11}e^{F_c\sigma_1}}\end{bmatrix}. \tag{18}$$

Correspondingly, $A_{ij}^{(1)}$ is satisfied by

$$A_{ij}^{(1)}=\begin{bmatrix}-\frac{(A_{13}^{(0)})^2}{A_{55}^{(0)}}\epsilon U_3' & -\frac{A_{13}^{(0)}A_{11}^{(0)}}{A_{55}^{(0)}}\epsilon U_3' & 0\\ -\frac{A_{13}^{(0)}A_{11}^{(0)}}{A_{55}^{(0)}}\epsilon U_3' & -\frac{2A_{11}^{(0)}}{A_{55}^{(0)}}\epsilon U_3' & 0\\ 0 & 0 & -A_{55}^{(0)}\epsilon U_1'\end{bmatrix}. \quad (19)$$

It is not hard to see that $B_{11}^*$ and $A_{11}^{(1)}$ as well as $B_{55}^*$ and $A_{55}^{(1)}$ have a similar estimating precision under the non-closure assumption of prestressed cracks.

Considering that $A_{ij}$ in the Padé AHM represents the effective stiffness matrix of stressed rocks with unclosed fractures, we can take its inverse as the drained compliance $S_{ij}^{\mathrm{drs}}$ of the reference rock. Therefore, the stress-dependent elastic compliance in the Padé AHM with the closure of cracks can be written as

$$\begin{cases}S_{ij}=\left(A_{ij}^{\text{Padé AHM}}\right)^{-1}+S_{ij}^*\\ A_{ij}=\left(S_{ij}\right)^{-1}\end{cases}, \quad (20)$$

where $A_{ij}^{\text{Padé AHM}}$ is calculated by equation (12) and $S_{ij}^*$ can be expressed as follows in 2D cases with an exponential term to describe the closure of cracks (Shapiro, 2017),

$$\begin{cases}S_{11}^*=S_{11}+F_c\phi_{11}e^{F_c\sigma_1}\\ S_{33}^*=S_{33}+F_c\phi_{33}e^{F_c\sigma_3}\\ S_{55}^*=S_{55}+F_c\left(\phi_{11}e^{F_c\sigma_1}+\phi_{33}e^{F_c\sigma_3}\right)/4\\ S_{13}^*=S_{13}\end{cases}. \quad (21)$$

## 3. Dispersion analyses with plane waves

Based on the general equation of motion for anisotropic media, the elastic wave equation for various acoustoelastic Hudson models (AHM, Padé AHM, and AHCM) can be expressed as

$$\begin{cases}A_{11}\frac{\partial^2 u_x}{\partial x^2}+A_{55}\frac{\partial^2 u_x}{\partial z^2}+(A_{13}+A_{55})\frac{\partial^2 u_z}{\partial x\partial z}+\rho f_x=\rho\frac{\partial^2 u_x}{\partial t^2}\\ A_{55}\frac{\partial^2 u_z}{\partial x^2}+A_{33}\frac{\partial^2 u_z}{\partial z^2}+(A_{13}+A_{55})\frac{\partial^2 u_x}{\partial x\partial z}+\rho f_z=\rho\frac{\partial^2 u_z}{\partial t^2}\end{cases}, \quad (22)$$

where $f$ denotes the components of the external body force. Let us assume that the displacement vector $\mathbf{u}$ is described by the following plane waves,

$$\mathbf{u}=\mathbf{U_0}\exp[\mathrm{i}\omega(\mathbf{n}\cdot\mathbf{x}-t)], \quad (23)$$

where $\mathbf{U_0}$ is the amplitude vector, $\omega$ is the angular frequency, $\mathbf{n}$ is the slowness vector, $\mathbf{x}$ is the position vector, and $\mathrm{i}=\sqrt{-1}$. For wave propagation in the *xoz* plane, we have $\mathbf{n}=(\sin\theta,0,\cos\theta)$ with $\theta$ the polar angle.

Substituting equations (23) into (22), we obtain the Christoffel equation,

$$\begin{bmatrix}\Gamma_{11}-\rho v^2 & \Gamma_{13}\\ \Gamma_{31} & \Gamma_{33}-\rho v^2\end{bmatrix}\begin{bmatrix}u_x\\ u_z\end{bmatrix}=0, \quad (24)$$

where

$$\begin{cases}\Gamma_{11}=A_{11}n_x^2+A_{55}n_z^2\\ \Gamma_{13}=\Gamma_{31}=(A_{13}+A_{55})n_xn_z.\\ \Gamma_{33}=A_{55}n_x^2+A_{33}n_z^2\end{cases} \quad (25)$$

Solving equation (24), we have

$$\begin{cases}v_{\mathrm{P}}(\theta)=\frac{1}{\sqrt{2\rho}}\sqrt{(A_{11}+A_{55})\sin^2\theta+(A_{33}+A_{55})\cos^2\theta+D(\theta)}\\ v_{\mathrm{SV}}(\theta)=\frac{1}{\sqrt{2\rho}}\sqrt{(A_{11}+A_{55})\sin^2\theta+(A_{33}+A_{55})\cos^2\theta-D(\theta)}\end{cases}, \quad (26)$$

with

$$D(\theta)=\sqrt{[(A_{11}-A_{55})\sin^2\theta-(A_{33}-A_{55})\cos^2\theta]^2+4(A_{13}+A_{55})^2\sin^2\theta\cos^2\theta}. \quad (27)$$

The fourth power and the square root in equation (27) generally are the source of considerable complexity. Furthermore, four elastic tensor elements are required for a full description of wave propagation in stressed fractured rocks. From equations (2) and (21), we see that these tensor elements can be calculated using the 2oeCs (i.e., $\lambda$ and $\mu$), the 3oeCs (i.e., $A$, $B$, and $C$), and the given fracture parameters.

### 3.1. Phase velocities in the AHCM for stressed fractured rocks

According to the acoustoelastic stiffness matrices for specific prestress conditions (confining, uniaxial, and pure-shear), we can calculate the background stiffness tensor $A_{ij}^{(0)}$ for Portland sandstone with the relevant properties (Winkler and Liu, 1996) as $\lambda=9.7$ GPa, $\mu=7.3$ GPa, $A=-1122$ GPa, $B=-419$ GPa, and $C=-340$ GPa. The embedded cracks with the density $\epsilon=0.2$ and the aspect ratio of 0.01 are oriented and perpendicular to the principal stress direction, where the VTI parameter model (Shapiro, 2017) is applied with $F_c=0.026\ \mathrm{MPa}^{-1}$, $\phi_{11}=0$, and $\phi_{33}=0.001$. Based on equation (25), we calculate the phase velocities as functions of both propagation angle (measured from the axis of symmetry) and prestress (under three typical prestress conditions) for the AHCM of stressed fractured rocks.

Figure 1 compares the qP and qSV velocities as functions of both angle and pressure for the isotropic background ($\epsilon=0$) under the confining, uniaxial, and pure-shear prestress conditions. 90° is the direction of the axis of symmetry (i.e., the direction of aligned fractures), whereas 0° is the direction of the uniaxial and pure-shear prestresses. As expected, both the waves show strong orthotropic feature under an anisotropic stress loading (i.e., uniaxial and pure-shear prestresses). It is worth noting that even for the isotropic background, the increasing velocity difference between the two axes with increasing anisotropic prestresses significantly enhances velocity anisotropy in Figure 1b. Unlike the uniaxial prestress condition, the absolute values of strains along the two axes of a pure-shear stress field are the same, implying that the stress-induced velocity anisotropy is more sensitive under the pure-shear prestress. From the velocity variations in Figure 1c, we see that qP and qSV waves could be decoupled at 30 MPa, but completely coupled each other at 50 MPa where the diagram of

qSV velocity becomes $\infty$, implying that the qSV velocity is 0 in the 90° direction along which we cannot observe the qSV wave. Acoustoelastic simulations of wavefield snapshots under various pure-shear prestresses (Yang et al., 2022a) confirm this feature.

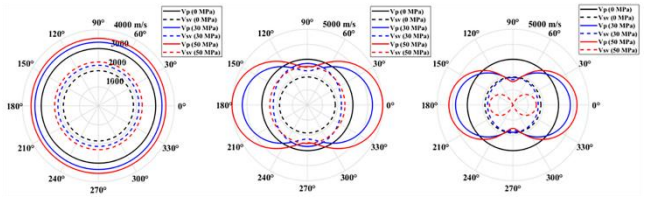

(a) (b) (c)

**Figure 1**. Comparison of P- and SV-wave velocities as functions of both angle and pressure for the AHCM of fractured rocks with $\epsilon = 0$ under the confining (a), uniaxial (b), and pure-shear (c) prestresses.

Figures 2 and 3 show the same example as Figure 1 except for fractured rocks with $\epsilon = 0.1$ and $\epsilon = 0.2$, respectively. Unlike the stress-induced anisotropic background shown in Figure 1, the involvement of fracture-induced anisotropy significantly enhances the complexity of velocity anisotropies in prestressed fractured rocks, especially under the anisotropic stress loading (i.e., uniaxial and pure-shear prestresses). Stress- and fracture-induced anisotropies exhibit different directionalities and are superimposed each other. With the increase of prestresses, we see obvious differential changes of qP and qSV velocities between the 0° and 90° directions. The resulting effective anisotropy will characterize wave propagation in such prestressed fractured rocks. As expected, the closure of cracks at 50 MPa under an anisotropic stress loading reduces the fracture-induced anisotropy and makes the stress-induced anisotropy become dominant.

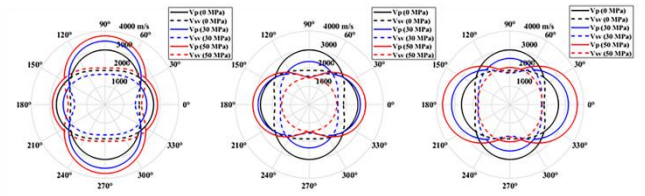

(a) (b) (c)

**Figure 2**. Same as Figure 1 for fractured rocks with $\epsilon = 0.1$.

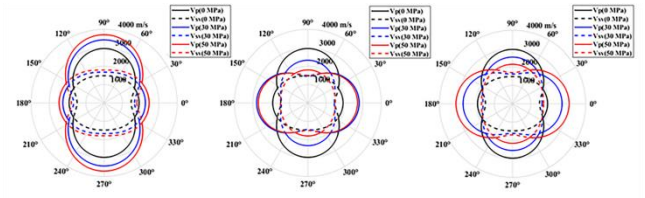

(a) (b) (c)

**Figure 3**. Same as Figure 1 for fractured rocks with $\epsilon = 0.2$.

### 3.2. Effective moduli for stressed fractured rocks with varying crack densities

The Hudson formulation is known to be valid for the crack density smaller than 0.1, whereas the Padé-approximation-based expansion can handle larger crack densities. However, prestresses tend to close compliant cracks, and hence could relax the effect of approximation. In order to understand the different behavior of various acoustoelastic Hudson models (AHM, Padé AHM, and AHCM), we calculate the elastic moduli as functions of both crack density and prestress for Portland sandstone using these acoustoelastic models based on the relevant 2oeCs and 3oeCs properties and crack parameters given in Section 3.1.

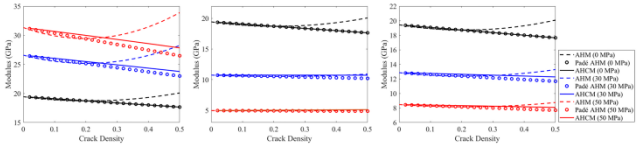

(a) (b) (c)

**Figure 4**. Comparison of the unnormalized elastic modulus $A_{11}$ calculated by AHM (dash line), Padé AHM (circle line), and AHCM (thick solid line) as functions of crack density and pressure for dry cracks under the confining (a), uniaxial (b), and pure-shear (c) prestresses.

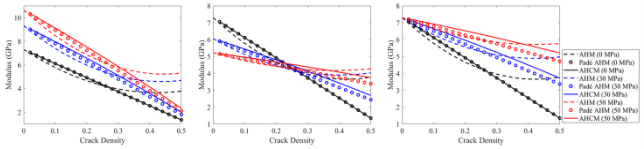

(a) (b) (c)

**Figure 5**. Same as Figure 4 but for $A_{55}$.

We compare the elastic moduli $A_{11}$ (Figures 4) and $A_{55}$ (Figures 5) calculated by AHM, Padé AHM, and AHCM, respectively, as functions of crack density and pressure for dry cracks under the confining, uniaxial, and pure-shear prestress conditions. We see that the accuracies of the AHM and Padé AHM conform to theoretical analysis. These effective elastic moduli generally decrease with increasing crack densities. However, the effect of prestresses depends on the prestress conditions. The confining prestress increases the effective elastic moduli where high prestresses further differentiate these models. Conversely, the anisotropic stress loading (i.e., uniaxial and pure-shear) reduces the effective elastic moduli because of the different directionalities between prestresses and crack normals, where high prestresses further assimilate these models. For the zero-pressure condition, both the AHCM and Padé AHM come to the same result.

## 4. Acoustoelastic Thomsen parameters for stressed fractured rocks

It is important to establish the analytic relationship between prestress modes and the resulting Thomsen parameters (Thomsen, 1986) that represent seismic anisotropy. Prestresses affect not only the velocity of waves but also their amplitude and propagation

direction (Yang et al., 2022b), which is strongly related to the orientations of both prestresses and fractures. As indicated by Sarkar et al. (2003), an isotropic solid subject to the uniaxial stress exhibits symmetry close to hexagonal. Numerical simulations of acoustoelastic waves (Yang et al., 2022a, 2023) demonstrate that the initially isotropic background is still isotropic if subject to the confining stress, but presents orthotropic feature under an anisotropic stress loading (uniaxial and pure-shear).

From equation (1), we see that the stress-induced orthotropic background $A_{ij}^{(0)}$ has the same matrix representation as the stiffness tensor (Tsvankin, 1997) for such orthotropic media induced by aligned fractures. We assume the waves polarized in the *xoz* plane, which is identical to the corresponding equation for vertical transverse isotropy. Therefore, we can follow the Thomsen-style notation of weak-anisotropy approximation (Tsvankin, 1997) to express the acoustoelastic stiffness tensor $A_{ij}^{(0)}$ as the following dimensionless Thomsen parameters that concisely characterize the stress-induced orthotropic background,

$$\begin{cases} v_{\mathrm{P}}^{(0)} = \sqrt{A_{33}^{(0)}/\rho} \\ v_{\mathrm{S}}^{(0)} = \sqrt{A_{55}^{(0)}/\rho} \\ \varepsilon^{(0)} = \frac{A_{11}^{(0)} - A_{33}^{(0)}}{2A_{33}^{(0)}} \\ \delta^{(0)} = \frac{\left(A_{13}^{(0)} + A_{55}^{(0)}\right)^2 - \left(A_{33}^{(0)} - A_{55}^{(0)}\right)^2}{2A_{33}^{(0)}\left(A_{33}^{(0)} - A_{55}^{(0)}\right)} \end{cases}, \tag{28}$$

where $v_{\mathrm{P}}^{(0)}$ and $v_{\mathrm{S}}^{(0)}$ are the background velocities of P and S waves, respectively, and the dimensionless parameters $\varepsilon^{(0)} = \varepsilon_2^{(0)}$ and $\delta^{(0)} = \delta_2^{(0)}$ represent the strength of anisotropies where the subscript refers to the *y*-axis direction that defines the orientation of the *xoz* symmetry plane. Extending to the whole fractured rocks, we obtain the effective Thomsen parameters of various acoustoelastic Hudson models (AHM, Padé AHM, and AHCM) that can be generally expressed as

$$\begin{cases} v_{\mathrm{P}} = \sqrt{A_{33}/\rho} \\ v_{\mathrm{S}} = \sqrt{A_{55}/\rho} \\ \varepsilon = \frac{A_{11} - A_{33}}{2A_{33}} \\ \delta = \frac{(A_{13} + A_{55})^2 - (A_{33} - A_{55})^2}{2A_{33}(A_{33} - A_{55})} \end{cases}. \tag{29}$$

We see that the four elastic tensor elements can be combined as the non-dimensional Thomsen parameters for a full description of wave propagation in stressed fractured rocks. Here, $v_{\mathrm{P}}$ and $v_{\mathrm{S}}$ could be regarded as vertical velocities. These effective Thomsen parameters reduce to zero in the case of isotropy and can be extracted from seismic data.

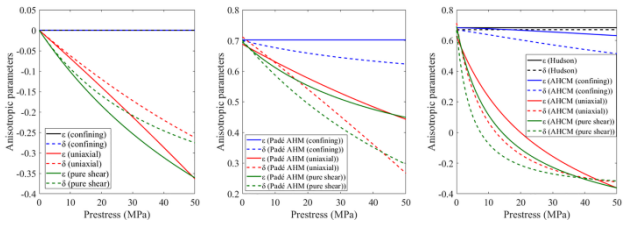


**Figure 6**. Comparison of the effective Thomsen parameters as a function of pressure between the stress-induced background orthotropy (left panel), the Padé AHM effective anisotropy (middle panel), and the AHCM effective anisotropy (right panel) of stressed fractured rocks under different prestress conditions.

We calculate the Thomsen parameters as a function of prestress for Portland sandstone based on the relevant 2oeCs and 3oeCs properties and crack parameters given in Section 3.1. The resulting background orthotropy, Padé AHM effective anisotropy, and AHCM effective anisotropy are shown in Figure 6 under different prestress conditions (confining, uniaxial, and pure-shear). We see that the confining prestress does not introduce any anisotropy into the background stiffness tensor $A_{ij}^{(0)}$, whereas the uniaxial and pure-shear prestresses significantly enhance the background anisotropy. More accurate results over $A_{ij}^{(0)}$ resort to the Padé AHM under the assumption of unclosed cracks with increasing prestress. In the right panel, as expected, the anisotropy parameters by the conventional HM (solid and dotted black lines) do not change with prestress. whereas the AHCM even under the confining prestress (solid and dotted blue lines) presents slight stress-dependent anisotropy because the anisotropy of aligned fractures is modified by prestress (possibly inducing the partial closure of cracks). The uniaxial and pure-shear prestresses tend to close aligned fractures along the vertical stress direction, reducing the effective anisotropy to 0 quickly at small prestresses. With increasing prestress further, the stress-induced background orthotropy becomes dominant.

It should be mentioned that under the stress-induced weak anisotropy approximation (Sarkar et al., 2003; Prioul et al., 2004), the stress-induced contribution is only limited to the isotropic background with the fracture-induced anisotropy remaining unchanged. The effective Thomsen parameters in equation (28) of stressed fractured rocks reduce to the following acoustoelastic Thomsen parameters (Sarkar et al., 2003),

$$\begin{cases} \varepsilon \approx \varepsilon^{(0)} + \tilde{\varepsilon} = \frac{K}{2A_{55}^{(0)}}(\tau_{11} - \tau_{33}) + \tilde{\varepsilon} \\ \delta \approx \delta^{(0)} + \tilde{\delta} = \frac{K}{2A_{55}^{(0)}}(\tau_{11} - \tau_{33}) + \tilde{\delta}' \end{cases}, \tag{30}$$

where $\tau_{11}$ and $\tau_{33}$ are the principal stresses. $\tilde{\varepsilon}$ and $\tilde{\delta}$ describe the unstressed anisotropy induced by aligned fractures. Figure 7 compares the effective Thomsen parameters calculated by the weak-

anisotropy model, the Padé AHM, and the AHCM, respectively. We see that these models demonstrate small differences for the confining prestress, but with large discrepancies occurring under the uniaxial and pure-shear prestresses. The AHCM anisotropy parameters show strong nonlinear changes especially at small prestress due to the gradual closure of cracks. With increasing prestress, the sensitivity of fractures to prestress gradually decreases, and the stress-induced background orthotropy becomes dominant. Unlike the AHCM, the weak-anisotropy model shows approximately linear changes.

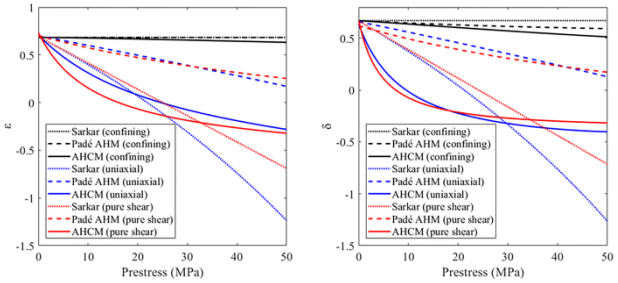


**Figure 7**. Comparison of the effective Thomsen parameters $\epsilon$ (left panel) and $\delta$ (right panel) as a function of pressure between the weak-anisotropy model, the Padé AHM, and the AHCM of stressed fractured rocks under different prestress conditions.

We use experiment data to verify the accuracy of the Padé AHM and AHCM proposed in this study. The experimental data used are obtained from Han et al. (2022) using a brine-saturated artificial sandstone with aligned penny-shaped cracks. Ultrasonic velocities in the artificial sandstone are measured under applied uniaxial prestress from 5 to 50 MPa. These aligned cracks significantly enhance the elastic anisotropy of fractured rocks. The artificial sandstone has the porosity 25.19 %, the density 1.98 g/cm$^3$, the bulk modulus $K = 3.588$ GPa, and the shear modulus $\mu = 6.9$ GPa. The non-cracked base material (quartz sand) has a density of 2.65 g/cm$^3$. Based on the P- and S-wave velocities of the rock without cracks under small prestress, we calculate the 3oeCs as $A = -1001$ GPa, $B = -421$ GPa, and $C = -300$ GPa by fitting the velocity-prestress curves. The aligned penny-shaped cracks have the crack density $\epsilon = 0.062$ with the generalized porosity $\phi_{11} = 0$ and $\phi_{33} = 0.001$.

Figure 8 compares the effective Thomsen parameters ($\varepsilon$ and $\delta$) as a function of uniaxial pressure estimated by the experimental data (Han et al., 2022), the weak-anisotropy model, the Padé AHM, and the AHCM, respectively. These curves are characteristic of linearity because of low crack density. As expected, the AHCM has a higher accuracy than other two models. The error with the experimental data at $P = 20$~$30$ MPa may be from the rock matrix itself caused by layered compaction during the preparation of artificial sandstone (Han et al., 2022).

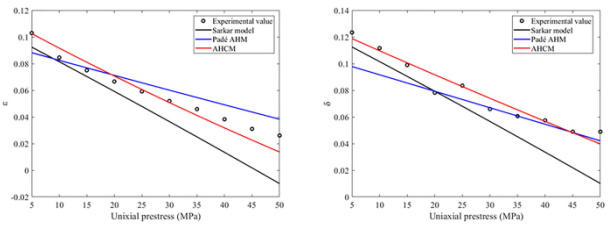


**Figure 8**. Comparison of the effective Thomsen parameters $\epsilon$ (left panel) and $\delta$ (right panel) as a function of uniaxial pressure between the experiment measurement, the weak-anisotropy model, the Padé AHM, and the AHCM.

## 5. Numerical simulations for wave propagation in stressed fractured rocks

In this section, acoustoelastic finite-difference simulations based on the AHCM stiffness matrix are performed for elastic wave propagation in stressed fractured media. A group of aligned fractures are embedded into an isotropic, homogeneous background medium, with the $z$-axis (i.e., symmetry axis) perpendicular to the strike of fractures. The resulting model has the same acoustoelastic properties and crack parameters as those of the brine-saturated artificial sandstone (Han et al., 2022) detailed in the previous section. We use a rotated staggered-grid finite-difference (RSG-FD) scheme (Saenger et al, 2000; Saenger and Shapiro, 2002) that is a robust tool for complex anisotropic media without the averaging of elastic moduli over rotated grids. The method has eighth-order (for the space derivatives) and second-order (for the time derivatives) accuracies and has been used by for acoustoporoelastic simulations of wave propagation in stressed solids (Yang et al., 2022a) and stressed porous rocks (Yang et al., 2022b). In this study, the RSG-FD scheme is applied to the first-order velocity-stress AHCM equation, which is detailed in Appendix A.

The source is a vertical force located at the center of the model with the time history,

$$s(t) = (t - t_0)e^{-[\pi f_0(t-t_0)]^2}, \qquad (31)$$

where the central frequency $f_0 = 1.42$ MHz, and $t_0$ is a delay time. According to equation (A-13) for the condition of stability, the maximum frequency $f_{\max} = 4f_0$ and $n_\lambda = 3$ (Chen et al., 2006), and we obtain $V_{\min} = 1704$ m/s. Considering the closure of cracks at a large prestress, we determine the maximum velocity $v_{\max}$ at the maximum prestress 50 MPa, but with $v_{\min}$ set at 0 MPa. From the parameters listed above, we can obtain $v_{\max} = v_P = 3528$ m/s at 50 MPa and $v_{\min} = v_S = 1848$ m/s at 0 MPa, which enables a time step of $2{\cdot}10^{-7}$ s and a grid size of $10^{-4}$ m to satisfy the condition of stability.

Figure 9 shows the wavefield snapshots at $t = 0.12$ ms for wave propagation in unstressed fractured rocks with different crack densities. At zero prestress, the AHCM stiffness matrix reduces to the Padé HM so that

the fracture-induced anisotropy dominates the shape feature of wavefronts. We see that the circular wavefronts at $\epsilon = 0.0$ (indicating the isotropic homogeneous background) become more and more flattened along the $z$-axis (perpendicular to the strike of fractures) with increasing crack densities. Wave propagation along the strike of fractures (i.e., the $x$-axis) has a faster speed than along the $z$-axis. These elliptical wavefronts due to anisotropic velocity represent the anisotropic characteristic of VTI media. Additionally, the azimuthal anisotropy of P wave is more obvious than that of S wave.

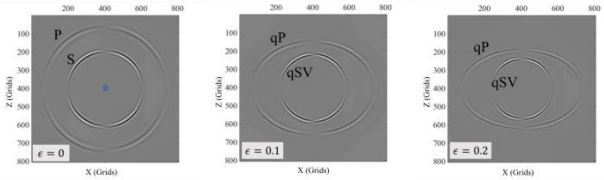


**Figure 9.** Wavefield snapshots at $t$ = 0.12 ms of the particle velocity ($x$-component) for wave propagation in unstressed fractured rocks with different crack densities.

Figure 10 shows the wavefield snapshots of stressed fractured rocks with $\epsilon = 0.1$ under different prestress conditions (confining, uniaxial, and pure-shear) at $P = 10$ MPa, with the numerical simulations using the Padé AHM without considering the closure of prestressed cracks. As expected from Figure 1a, the confining prestress only increases the background velocity without stress-induced anisotropy. The uniaxial and pure-shear prestresses are loaded along the $z$-axis (perpendicular to the strike of fractures) so that the stress-induced background anisotropy has the same symmetry axis as the fracture-induced anisotropy. However, both the anisotropies cancel each other because the uniaxial prestress increases the velocity along the $z$-axis, whereas the strike of fractures enhances velocity along the $x$-axis. Therefore, the wavefronts under the anisotropic prestress become less flattened along the $z$-axis than those in Figure 9.

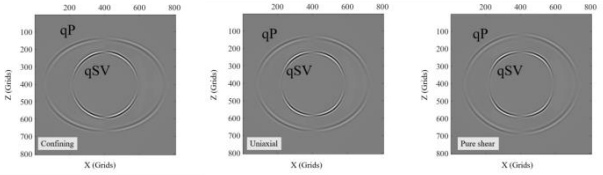


**Figure 10.** Wavefield snapshots at $t$ = 0.12 ms of the particle velocity ($x$-component) for wave propagation in stressed fractured rocks with $\epsilon = 0.1$ under different prestress conditions (confining, uniaxial, and pure-shear) at $P = 10$ MPa, with the numerical simulation using the Padé AHM without considering the closure of stressed cracks.

Figure 11 shows the same wavefield snapshots as Figure 9 but with the numerical simulations using the AHCM that considers the closure of stressed cracks. As expected, the anisotropic prestress (uniaxial and pure-shear) makes the aligned fractures more likely to close and further reduces the fracture-induced anisotropy. The elliptical wavefronts become more circular than those in Figure 10 and the stress-induced background anisotropy increases to neutralize the fracture-induced anisotropy. With increasing prestress further, as shown in Figure 12, the nearly circular wavefronts at $P = 10$ MPa become more and more flattened along the $x$-axis (parallel to the strike of fractures). the stress-induced background anisotropy dominates the shape feature of wavefronts. In conclusion, the effective anisotropy of stressed fractured rocks depends on fracture orientation, crack density, prestress mode and magnitude, and loading direction.

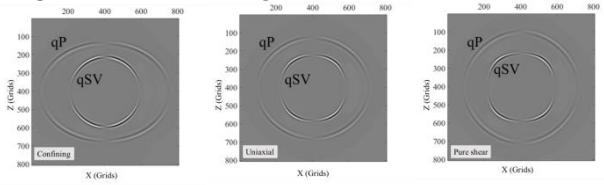


**Figure 11.** Same as Figure 10 but with the numerical simulation using the AHCM that considers the closure of stressed cracks.

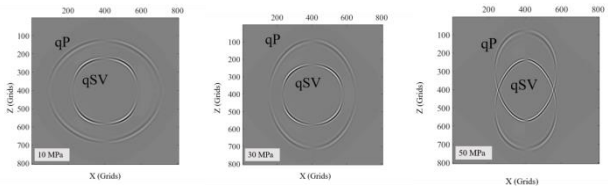


**Figure 12.** Wavefield snapshots at $t$ = 0.12 ms of the particle velocity (x-component) for wave propagation in prestressed fractured rocks with $\epsilon = 0.1$ under different uniaxial pressures, with the numerical simulation using the AHCM that considers the closure of stressed cracks.

## 6. Discussion

The Earth's interior is generally subjected to tectonic stress that often induces fractures in crustal rocks. Seismic-wave velocity and attenuation are sensitive to stress in most fractured rocks because of their compliant behavior over the background matrix. Such stress-induced incremental deformations with increasing prestress mostly undergo nonlinear elastic (due to the closure of compliant pores), hyperelastic (due to the residual stress accumulated), and inelastic (due to fracture growth) deformations prior to mechanical failure. Wave propagation in such stressed fractured rocks involves the complex interaction of fracture-induced anisotropy, stress-induced anisotropy, and stress-induced crack closure. In this article, we restrict the scope to the first two deformations. The acoustoelastic 3oeCs (Green, 1973; Pao and Gamer, 1985; Grinfeld and Norris, 1996), strictly valid for an isotropic homogeneous medium, only account for the stress-induced background anisotropy due to hyperelasticity created by the residual stress that accumulated during the closure of cracks. Hudson's (1980, 1981) and Cheng's (1993) effective media theories only account for fracture-induced anisotropy

without regard to the effect of external pressure. The stress-induced crack closure has been extensively addressed based on various microcrack models (e.g., Shapiro, 2003; David and Zimmerman, 2012; Shapiro, 2017). The Padé acoustoelastic 3oeCs (Fu and Fu, 2017; Zheng et al., 2024) take into account both the stress-induced closure of cracks and the stress-induced background anisotropy, which, however like the conventional acoustoelastic 3oeCs, are formulated from the strain energy function of isotropic rocks by ignoring the fracture-induced anisotropy. In this article, we focus on both the stress-induced nonlinear elastic and hyperelastic deformations of fractured rocks. We combine the traditional acoustoelasticity, the Hudson/Cheng models, and the dual-porosity model to address the coupled anisotropies of stressed fractured rocks. For this purpose, we have to assure the consistency of assumptions and limitations applied to these theories during the deformation process.

The Hudson/Cheng models represent an abstract model with a spatially homogeneous distribution of aligned cracks, which significantly simplify real fractures by rigorous assumptions and limitations (Mavko et al., 2009). Real fractures have irregular shapes with some closed or interconnected partially, grossly violating the basic theoretical assumption of isolated, penny-shaped cracks. However, these details of fracture microgeometry turn out to be unimportant for the effective elasticity given a typical noise level in seismic data (Grechka and Kachanov, 2006). Stress-induced closure characteristics vary significantly among individual cracks, depending on loading direction, crack orientation, shape, surface roughness, and on the nature of fracture intersections and interactions (Batzle et al., 1980). Low aspect-ratio cracks close at relatively low pressures. At some intersections, one fracture would close while another simultaneously opens, depending upon their orientations relative to the applied stress. Yet, a large number of rock-physics experiments on fractured rocks under the confining/uniaxial moderate pressures, accumulated in the past decades, show that the resulting stress-strain curves mostly present an initial nonlinear segment due to the closure of compliant pores, followed by an almost linear segment due to the accumulated residual stress inside the background matrix. In a word, prestress first tends to close compliant pores with elastic nonlinearity, reducing crack densities and fracture anisotropies, and hence could mitigate the assumptions and limitations applied to the Hudson/Cheng models. Then, hyperelastic deformations are dominant with linear strains (via displacements) (Sinha and Plona, 2001) where the acoustoelastic 3oeCs can be applicable. Therefore, the proposed AHM, Padé AHM, and AHCM in this article have their assumptions and limitations consistent with those by the Hudson/Cheng models. In addition, stress conduction in rocks is a very slow process relative to wave propagation. Wave-induced small disturbances are superposed onto elastically deforming cracks instantly in the sense that the time scale of seismic waves is much short compared to the time scale required for stress equilibration, that is, the stress-induced deformation process would not affect the applicability of these acoustoelastic Hudson/Cheng models.

In this article, much attention is paid to the coupling process of different anisotropies during wave propagation, but with many other important issues largely unaddressed. Dynamic stress interaction across cracks during wave propagation is an important issue that cannot be neglected. Fjær et al. (2021) give a simple example to show that the spatial arrangement of cracks decides the dependence of stiffness on crack density, as much as the crack density itself. Stress shielding and amplification due to wave propagation in unpressurized cracks have been extensively studied (e.g., Hu and McMechan, 2009; Zhao et al., 2015; Cao et al., 2019, 2020). Such stress interactions significantly affect the fracture stiffness tensor (Grechka and Tsvankin, 2003). Prestress across cracks would further enhance stress interaction before their closure, causing the softening and stiffening of fractures (Liu and Fu, 2021; Liu et al., 2021), which should be considered in the acoustoelastic stiffness tensor for wave propagation in stressed fractured rocks. Fracture-induced scattering attenuation is another important issue (e.g., Fang et al., 2013; Zhou et al., 2023; Feng et al., 2023) that cannot be neglected because of its potential applications in crack detection (Fehler et al., 1998; Zheng et al., 2013; Fang et al., 2014; Hu et al., 2018a). Such a scattering sensitivity is strongly related to wavelengths comparable to the scale of fractures (Wu, 1989). Prestress-enhanced scattering attenuation has been extensively studied with experimental measurements (Guo and Fu, 2007; Hu et al., 2018b) and numerical simulations (Zhang et al., 2014; Wei and Fu, 2014; Zhou et al., 2021) of porous rocks. A comprehensive investigation of scattering attenuation in stressed rocks with compliant pores has been made by comparison of experimental measurements, acoustoporoelastic predictions, and numerical simulations (Fu et al., 2020) where the dual-porosity model (Shapiro, 2003) is incorporated into the acoustoporoelastic 3oeCs for describing the stress dependency of compliant pores. Generally speaking, the stress-enhanced scattering attenuation of fractured rocks could be handled naturally by the acoustoelastic Hudson/Cheng models proposed in this study. The aforementioned dynamic stress interaction and enhanced scattering attenuation across stressed cracks are two important topics to be approached in the future.

## 7. Conclusion

As an active field of research, the seismic response

of fractured rocks has been extensively assessed in the framework of the theory of seismic anisotropy mostly without considering the presence of prestress. Prestress tends to dominate the mechanical properties of fractured rocks due to the stress-induced anisotropy and crack compliant behavior over the background matrix. Therefore, the effective anisotropy for wave propagation in pressed fractured rocks involves a complex coupling process of fracture- and stress-induced anisotropies. Both change reciprocally with increasing prestress, significantly relevant to crack density and orientation, prestress mode and magnitude, and loading direction.

We incorporate acoustoelasticity into the Hudson/Cheng anisotropic model to address this issue, resulting in the AHM, Padé AHM, and AHCM with different accuracies and computational complexities to approach the coupled anisotropies. We conduct the plane-wave analysis of phase velocities and calculate the effective moduli of stressed fractured rocks with varying crack densities in order to determine the accuracy of these theoretical models under the isotropic (confining) and anisotropic (uniaxial and pure-shear) prestresses. The effective Thomsen parameters of these models are formulated and applied to experimental data with stressed fractured rocks, where the comparison with the weak-anisotropy model validates the accuracy of various acoustoelastic Hudson models. Finite-difference numerical simulations are implemented to solve the first-order velocity-stress formulations of Padé AHM, and AHCM equations for wave propagation in stressed fractured media under different types of prestresses. Numerical examples of wavefield snapshots differentiate the contribution of different anisotropies through the variety of the shapes of wavefronts.

The proposed AHM, Padé AHM, and AHCM describe the coupled anisotropies. As expected from the traditional Hudson/Cheng anisotropic models, the AHM is valid for the crack density smaller than 0.1, the Padé AHM could handle the crack density up to 0.3, and the AHCM extends the Padé AHM to consider the stress-induced closure of cracks by incorporating the dual-porosity model. The coupled anisotropies are strongly related to the relativity between the fracture strike and the loading direction. For the fracture-induced anisotropy, the maximum speed is along the strike of fractures, whereas for the stress-induced background anisotropy, the maximum speed is along the loading direction. The isotropic (confining) prestress evenly changes the background velocity without stress-induced background anisotropy. In such an isotropic prestress, cracks are hard to be closed. Therefore, the fracture-induced anisotropy dominates wave propagation in stressed fracture rocks. For the anisotropic (uniaxial and pure-shear) prestress, the coupled anisotropies will be enhanced if the strike of fractures is oriented in the loading direction, whereas both the anisotropies cancel each other if the loading direction is perpendicular to the strike of fractures. However, if we consider the stress-induced closure of cracks, the anisotropic prestress makes the aligned fractures more likely to close and further reduces the fracture anisotropy while the background anisotropy will dominate the shape feature of wavefronts with increasing prestress. In conclusion, the effective anisotropy of stressed fractured rocks depends on fracture orientation, crack density, prestress mode and magnitude, and loading direction.

### Acknowledgements

This work was supported in part by the National Natural Science Foundation of China under Grant 42230803 and Grant 41821002 and in part by the 111 Project “Deep-Superdeep Oil and Gas Geophysical Exploration” under Grant B18055.

## Appendix A

### Acoustoelastic RSG-FD numerical scheme applied to the first-order velocity-stress formulation of Padé AHM or AHCM equations

The first-order velocity-stress formulation of 2D acoustoelastic equations can be generally expressed as (Yang et al., 2022a)

$$\begin{cases} \rho v_{x,t} = \tau_{xx,x} + \tau_{xz,z}, \\ \rho v_{z,t} = \tau_{xz,x} + \tau_{zz,z}, \\ \tau_{xx,t} = A_{11} v_{x,x} + A_{13} v_{z,z}, \\ \tau_{zz,t} = A_{31} v_{x,x} + A_{33} v_{z,z}, \\ \tau_{xz,t} = A_{55}\left(v_{x,z} + v_{z,x}\right), \end{cases} \tag{A-1}$$

where the stiffness matrix $A_{ij}$ can be replaced by the counterpart of Padé AHM or AHCM equations.

### Rotated staggered grids

The RSG-FD method defines all the velocity components in one grid and all the stress components and elastic parameters in another grid, as described in Saenger and Shapiro (2002). For the stress update, the average over adjacent grid points is not required for the determination of shear modulus and other elastic parameters. The average densities over adjacent grid points are only needed for the velocity update.

As introduced by Saenger and Shapiro (2002) for the discretization of derivatives in the 2D case, the directions of spatial derivatives for the grid spacings $\Delta x$ and $\Delta z$ is rotated from the horizontal ($\mathbf{x}$) and the vertical ($\mathbf{z}$) directions to the diagonal directions ($\bar{\mathbf{x}}$ and $\bar{\mathbf{z}}$) by

$$\begin{cases} \bar{\mathbf{x}} = \frac{\Delta x}{h}\mathbf{x} - \frac{\Delta z}{h}\mathbf{z}, \\ \bar{\mathbf{z}} = \frac{\Delta x}{h}\mathbf{x} + \frac{\Delta z}{h}\mathbf{z}, \end{cases} \tag{A-2}$$

where $h = \sqrt{\Delta x^2 + \Delta z^2}$. The spatial derivatives in the

old horizontal and vertical directions can be rotated according to Eq. (A-2) through the derivatives' linear combination in the new diagonal directions,

$$\begin{cases} \frac{\partial}{\partial x} = \frac{h}{2\Delta x}\left(\frac{\partial}{\partial \bar{z}} + \frac{\partial}{\partial \bar{x}}\right), \\ \frac{\partial}{\partial z} = \frac{h}{2\Delta z}\left(\frac{\partial}{\partial \bar{z}} - \frac{\partial}{\partial \bar{x}}\right). \end{cases} \tag{A-3}$$

We can define the differential operators $D_{\bar{x}}$ and $D_{\bar{z}}$, which implement the spatial derivatives along diagonal directions ($\bar{\mathbf{x}}$ and $\bar{\mathbf{z}}$) in the time domain (Saenger et al., 2000),

$$\begin{cases} D_{\bar{x}}u(x,z,t) = \frac{1}{h}\left[u\left(x - \frac{\Delta x}{2}, z + \frac{\Delta z}{2}, t\right) - u\left(x + \frac{\Delta x}{2}, z - \frac{\Delta z}{2}, t\right)\right], \\ D_{\bar{z}}u(x,z,t) = \frac{1}{h}\left[u\left(x + \frac{\Delta x}{2}, z + \frac{\Delta z}{2}, t\right) - u\left(x - \frac{\Delta x}{2}, z - \frac{\Delta z}{2}, t\right)\right]. \end{cases} \tag{A-4}$$

With Eqs. (A-3) and (A-4), the numerical differentiation operators are obtained that allow us to compute the spatial derivatives along the $\mathbf{x}$ and $\mathbf{z}$ directions in the rotated staggered grid by a linear combination of the derivatives along the $\bar{\mathbf{x}}$ and $\bar{\mathbf{z}}$ directions,

$$\begin{cases} \frac{\partial}{\partial x}u(x,z,t) \approx \frac{h}{2\Delta z}[D_{\bar{x}}u(x,z,t) + D_{\bar{z}}u(x,z,t)], \\ \frac{\partial}{\partial z}u(x,z,t) \approx \frac{h}{2\Delta x}[D_{\bar{x}}u(x,z,t) - D_{\bar{z}}u(x,z,t)]. \end{cases} \tag{A-5}$$

## Finite-difference scheme

The first-order spatial derivatives for the stress and velocity components with $L$-order accuracy can be calculated by

$$v_{i,x}(x,z) \approx \sum_{n=1}^{L/2} \frac{c_n}{2\Delta x}\{v_i(x + (n-1/2)\Delta x, z + (n-1/2)\Delta z) + v_i(x + (n-1/2)\Delta x, z - (n-1/2)\Delta z) - v_i(x - (n-1/2)\Delta x, z - (n-1/2)\Delta z) - v_i(x - (n-1/2)\Delta x, z + (n-1/2)\Delta z)\}, \tag{A-6}$$

$$v_{i,z}(x,z) \approx \sum_{n=1}^{L/2} \frac{c_n}{2\Delta z}\{v_i(x + (n-1/2)\Delta x, z + (n-1/2)\Delta z) - v_i(x + (n-1/2)\Delta x, z - (n-1/2)\Delta z) - v_i(x - (n-1/2)\Delta x, z - (n-1/2)\Delta z) + v_i(x - (n-1/2)\Delta x, z + (n-1/2)\Delta z)\}, \tag{A-7}$$

$$\tau_{ij,x}(x + \Delta x/2, z + \Delta z/2) \approx \sum_{n=1}^{\frac{L}{2}} \frac{c_n}{2\Delta x}\{\tau_{ij}(x + n\Delta x, z + n\Delta z) + \tau_{ij}(x + n\Delta x, z - (n-1)\Delta z) - \tau_{ij}(x - n\Delta x, z - (n-1)\Delta z) - \tau_{ij}(x - n\Delta x, z + n\Delta z)\}, \tag{A-8}$$

and

$$\tau_{ij,z}(x + \Delta x/2, z + \Delta z/2) \approx \sum_{n=1}^{\frac{L}{2}} \frac{c_n}{2\Delta z}\{\tau_{ij}(x + n\Delta x, z + n\Delta z) - \tau_{ij}(x + n\Delta x, z - (n-1)\Delta z) - \tau_{ij}(x - n\Delta x, z - (n-1)\Delta z) + \tau_{ij}(x - n\Delta x, z + n\Delta z)\}, \tag{A-9}$$

where $c_n$ are the differential coefficients. For the eighth-order spatial FD approximations, we have $c_1 = \frac{1225}{1024}$, $c_2 = -\frac{245}{3072}$, $c_3 = \frac{49}{5120}$, and $c_4 = -\frac{5}{7168}$ (Kindelan et al., 1990). In addition, we apply the CPML boundary method (Komatitsch and Martin, 2007; Martin and Komatitsch, 2009) to the numerical implementation to eliminate the interference of artificial boundary reflections.

For the second-order accuracy in time, we have the time difference formulations of the coupled acoustoelastic equations,

$$\begin{cases} v_x^{t+\frac{\Delta t}{2}}(x + \frac{\Delta x}{2}, z + \frac{\Delta z}{2}) = v_x^{t-\frac{\Delta t}{2}}(x + \frac{\Delta x}{2}, z + \frac{\Delta z}{2}) + dt(\tau_{xx,x}(x,z) + \tau_{xz,z}(x,z))/\rho, \\ v_z^{t+\frac{\Delta t}{2}}(x + \frac{\Delta x}{2}, z + \frac{\Delta z}{2}) = v_z^{t-\frac{\Delta t}{2}}(x + \frac{\Delta x}{2}, z + \frac{\Delta z}{2}) + dt(\tau_{xz,x}(x,z) + \tau_{zz,z}(x,z))/\rho, \\ \tau_{xx}^{t+\Delta t}(x,z) = \tau_{xx}^{t}(x,z) + dt(A_{11}v_{x,x}(x + \frac{\Delta x}{2}, z + \frac{\Delta z}{2}) + A_{13}v_{z,z}(x + \frac{\Delta x}{2}, z + \frac{\Delta z}{2}))/\rho, \\ \tau_{zz}^{t+\Delta t}(x,z) = \tau_{zz}^{t}(x,z) + dt(A_{31}v_{x,x}(x + \frac{\Delta x}{2}, z + \frac{\Delta z}{2}) + A_{33}v_{z,z}(x + \frac{\Delta x}{2}, z + \frac{\Delta z}{2}))/\rho, \\ \tau_{xz}^{t+\Delta t}(x,z) = \tau_{xz}^{t}(x,z) + dt(A_{55}v_{x,x}(x + \frac{\Delta x}{2}, z + \frac{\Delta z}{2}))/\rho. \end{cases} \tag{A-10}$$

## Stability analysis

The stability criterion for the velocity–stress RSG-FD operator with equal grid spacings can be generally expressed as the following inequality (Masson et al., 2006),

$$\frac{\Delta t V_{\max}}{h} \le C, \tag{A-11}$$

with

$$C = \frac{1}{\sqrt{D}\sum_{k=1}^{n}|c_n|}, \tag{A-12}$$

where $V_{\max}$ represents the maximum phase velocity in the medium, $D$ represents the spatial dimension, and $c_n$ are the differential coefficients depending on the order of the spatial operator. For an eighth-order spatial and second-order temporal 2D FD operators with coefficients $c_1 = \frac{1225}{1024}$, $c_2 = -\frac{245}{3072}$, $c_3 = \frac{49}{5120}$, and $c_4 = -\frac{5}{7168}$, we can calculate $C$=0.5497.

Numerical dispersion is one of the main factors affecting the accuracy of the finite-difference method. To reduce the level of numerical dispersions in the RSG-FD method, a discretization interval should be selected to ensure a good number of grid points $n_\lambda$ per minimum wavelength, which is generally calculated by

$$n_\lambda = \frac{V_{\min}}{h f_{\max}}, \tag{A-13}$$

where $V_{\min}$ is the minimum phase velocity and $f_{\max}$ is the maximum frequency, usually taken as four times the center frequency of the source. Dispersion errors accumulate with increasing propagation distances, which can be reduced by refining grids. Numerical experiments by Chen et al. (2006) show that no less than 3 grid points per wavelength are required for the RSG eighth-order operator.

## REFERENCES

Adams, L. H., and Williamson, E. D. (1923). On the compressibility of minerals and rocks at high pressures. ***Journal of the Franklin Institute***, 195(4), 475-529. doi: 10.1016/S0016-0032(23)90314-5.

Ba, J., Carcione, J. M., Cao, H., Yao, F. C., and Du, Q. Z. (2013). Poro-acoustoelasticity of fluid-saturated rocks. ***Geophysical Prospecting***, 61(3), 599–612.

Bakulin, A., Grechka, V., and Tsvankin, I. (2000). Estimation of fracture parameters from reflection seismic data—Part I: HTI model due to a single fracture set. ***Geophysics***, 65(6), 1788-1802.

Batzle, M. L., Simmons, G., and Siegfried, R. W. (1980). Microcrack closure in rocks under stress: Direct observation. ***Journal of Geophysical Research: Solid Earth***. 85(B12), 7072-7090.

Cao, C. H., Chen, F. Y., Fu, L.-Y., Ba, J., and Han, T. C. (2020). Effect of stress interactions on anisotropic P-SV-wave dispersion and attenuation for closely spaced cracks in saturated porous media. ***Geophysical Prospecting***, 68(8), 2536-2556.

Cao, C. H., Fu, L.-Y., Ba, J., and Zhang, Y. (2019). Frequency- and incident-angle-dependent P-wave properties influenced by dynamic stress interactions in fractured porous media. ***Geophysics***, 84(5), MR173-MR184. doi: 10.1111/1365-2478.1

Cao, Z., Wang, K., and Ma, Z. (2004). Acoustoelastic effects on guided waves in a fluid-filled pressurized borehole in a prestressed formation. ***The Journal of the Acoustical Society of America***, 116(3), 1406-1415.

Chen, H., Wang, X., and Lin, W. (2006). Parallel numerical simulation of the ultrasonic waves in a prestressed formation. ***Ultrasonics*** 44, e1013-e1017.

Cheng, C. H. (1993). Crack models for a transversely isotropic medium. ***Journal of Geophysical Research: Solid Earth***, 98(B1), 675-684.

Cheng, C. H., and Toksöz, M. N. (1979). Inversion of seismic velocities for the pore aspect ratio spectrum of a rock. ***Journal of Geophysical Research: Solid Earth***. 84(B13), 7533-7543.

David, E. C. and Zimmerman, R. W. (2012). Pore structure model for elastic wave velocities in fluid-saturated sandstones. ***Journal of Geophysical Research: Solid Earth***, *117*(B7), B07210.

Eshelby, J. D. (1957). The determination of the elastic field of an ellipsoidal inclusion, and related problems. ***Proc. R. Soc. London, Ser. A***, 241, 376-396.

Fang, X., Fehler, M., Zhu, Z., Chen, T., Brown, S., Cheng, A., and Toksöz, M. N. (2013). An approach for predicting stress-induced anisotropy around a borehole stress-induced anisotropy. ***Geophysics***, 78(3), D143-D150.

Fang, X., Fehler, M. C., Zhu, Z. (2014). Reservoir fracture characterization from seismic scattered waves. ***Geophysical Journal International***, 196(1), 481-492.

Fehler, M., House, L., and Phillips, W. S. (1998). A method to allow temporal variation of velocity in travel-time tomography using microearthquakes induced during hydraulic fracturing. ***Tectonophysics***, 289(1-3), 189-201.

Feng, Y. L., Wei, W., Fu, B. Y., and Fu, L.-Y. (2023). Seismic resolution analysis of subwavelength-scale cracks. ***Chinese Journal of Geophysics*** (in Chinese), DOI: 10.6038/cjg2023Q0822

Fjær, E., Holt, R. M., Horsrud, P., Raaen, A.M., and Risnes, R. (2021). ***Petroleum related rock mechanics (3rd ed.)***, Amsterdam and Oxford: Elsevier.

Fu, B. Y. and Fu, L.-Y. (2017). Poro-acoustoelastic constants based on Padé approximation. ***The Journal of the Acoustical Society of America***. 142(5), 2890-2904.

Fu, B. Y. and Fu, L.-Y. (2018). Poro-acoustoelasticity with compliant pores for fluid-saturated rocks. ***Geophysics***, 83(3), WC1-WC14.

Fu, B. Y., Fu, L.-Y., Deng, W. B., and Han, T. C. (2023a). Acoustoelastic Mori–Tanaka model for third-order elastic constants of fractured rocks. ***Geophysics***, *88*(4), MR211-MR228.

Fu, B. Y. and Fu, L.-Y. (2023b). Acoustoelastic DZ-MT model for stress-dependent elastic moduli of fractured rocks. ***International Journal of Rock Mechanics and Mining Sciences,*** in review.

Fu, L.-Y., Fu, B. Y., Sun, W., Han, T., and Liu, J. (2020). Elastic wave propagation and scattering in prestressed porous rocks. ***Science China Earth Sciences***, 63(9), 1309-1329.

Goldberg, Z. A. (1961). Interaction of plane longitudinal and transverse elastic waves. ***Soviet Physics Acoustics***, 6, 306–310.

Grechka, V. and Tsvankin, I. (2003). Feasibility of seismic characterization of multiple fracture sets. ***Geophysics***, 68, 1399–1407. doi: 10.1190/1 .1598133.

Grechka, V. and Kachanov, M. (2006). Effective elasticity of rocks with closely spaced and intersecting cracks. ***Geophysics***, 71(3), D85-D91.

Green R. E. (1973) ***Ultrasonic investigation of mechanical properties: in Treatise on Materials Science and Technology***, Academic Press, New York, Vol. 3.

Grinfeld, M. A. and Norris, A. N. (1996). Acoustoelasticity theory and applications for fluid-saturated porous media. ***The Journal of the Acoustical Society of America***, 100(3), 1368-1374.

Guo, M. Q. and Fu, L.-Y. (2007). Stress associated coda attenuation from ultrasonic waveform measurements. ***Geophys Res Lett***, 34, L09307.

Han, T., Yan, H., Li, B., and Fu, L.-Y. (2022). Pressure-dependent joint elastic–electrical properties in brine-saturated artificial sandstones with aligned penny-shaped cracks—Part I: Experimental results. ***Geophysical Journal International***, 228(2), 1071-1082.

Helbig, K. and Thomsen, L. (2005). 75-plus years of anisotropy in exploration and reservoir seismics: A historical review of concepts and methods. ***Geophysics***, 70 (6), 9ND-23ND.

Hu, Y. and McMechan, G. A. (2009). Comparison of effective stiffness and compliance for characterizing cracked rocks. ***Geophysics***, 74(2), D49–D55, doi: 10.1190/1.3073004.

Hu, H., Zheng, Y. C., Fang, X. D. (2018a). 3D seismic characterization of fractures with random spacing using the double-beam method. ***Geophysics***, 83(5), M63-M74.

Hu, J.H., Fu, L.-Y., Wei, W., and Zhang, Y. (2018b). Stress-

associated intrinsic and scattering attenuation from laboratory ultrasonic measurements on shales. ***Pure Appl Geophys***, 175: 929–962.

Hudson, J. A. (1980). Overall properties of a cracked solid. In ***Mathematical Proceedings of the Cambridge Philosophical Society*** (Vol. 88, No. 2, pp. 371-384). Cambridge University Press.

Hudson, J. A. (1981). Wave speeds and attenuation of elastic waves in material containing cracks. ***Geophysical Journal International***, 64(1), 133-150.

Jaeger, J. C., Cook, N. G. W., and Zimmerman, R. W. (2007). ***Fundamentals of rock mechanics***: Blackwell Publishing.

Johnson, P. A. and Rasolofosaon, P. N. J. (1996). Nonlinear elasticity and stress-induced anisotropy in rock. ***Journal of Geophysical Research: Solid Earth***, 101(B2), 3113-3124.

Johnson, P. A. and Shankland, T. J. (1989). Nonlinear generation of elastic waves in granite and sandstone: Continuous wave and travel time observations. ***Journal of Geophysical Research: Solid Earth***, 94(B12), 17729-17733.

Kindelan, M., Kamel, A., and Sguazzero, P. (1990). On the construction and efficiency of staggered numerical differentiators for the wave equation. ***Geophysics***, 55(1), 107-110.

Komatitsch, D. and Martin, R. (2007). An unsplit convolutional perfectly matched layer improved at grazing incidence for the seismic wave equation. ***Geophysics***, 72(5), SM155-SM167.

Lei, T., Sinha, B. K., and Sanders, M. (2012). Estimation of horizontal stress magnitudes and stress coefficients of velocities using borehole sonic data. ***Geophysics***, 77(3), WA181-WA196.

Ling, W., Ba, J., Carcione, J. M., and Zhang, L. (2021). Poroacoustoelasticity for rocks with a dual-pore structure. ***Geophysics***, *86*(1), MR17-MR25.

Liu, Q. H. and Sinha, B. K. (2000). Multipole acoustic waveforms in fluid filled boreholes in biaxially stressed formations: A finite-difference method. ***Geophysics***, 65, 190–201, doi: 10.1190/1.1444710.

Liu, N. and Fu, L.-Y. (2021). Modeling seismic responses in complex fractured media using the modified lattice spring model coupled with discrete fracture networks. ***Journal of Natural Gas Science and Engineering***, 95, 104206. DOI: 10.1016/j.jngse.2021.104206.

Liu, N. Li, Y. Y., Fu, L.-Y., Kong, Y., and Li, W. S. (2021). Integrated LSM-DFN modeling of naturally fractured reservoirs: Roughness effect on elastic characteristics. ***Pure and Applied Geophysics***, 178(3):1761-1779.

Martin, R. and Komatitsch, D. (2009). An unsplit convolutional perfectly matched layer technique improved at grazing incidence for the viscoelastic wave equation. ***Geophysical Journal International***, 179(1), 333-344.

Masson, Y. J., Pride, S. R., and Nihei, K. T. (2006). Finite difference modeling of Biot's poroelastic equations at seismic frequencies. ***Journal of Geophysical Research: Solid Earth***, 111(B10).

Mavko, G., Mukerji, T., and Dvorkin, J. (2009). ***The rock physics handbook: Tools for seismic analysis of porous media.*** Cambridge University Press.

Meegan Jr, G. D., Johnson, P. A., Guyer, R. A., and McCall, K. R. (1993). Observations of nonlinear elastic wave behavior in sandstone. ***The Journal of the Acoustical Society of America***, 94(6), 3387-3391.

Nishizawa, O. (1982). Seismic velocity anisotropy in a medium containing oriented cracks transversely isotropic case. ***Journal of Physics of the Earth***, 30(4), 331-347.

Norris, A. N. (1983). Propagation of plane waves in a pre-stressed elastic medium. ***The Journal of the Acoustical Society of America***, 74(5), 1642-1643.

Nur, A., and Simmons, G. (1969). Stress-induced velocity anisotropy in rock: An experimental study. ***Journal of Geophysical Research: Solid Earth***, 74, 6667–6674.

Pao, Y.-H. and Gamer, U. (1985). Acoustoelastic waves in orthotropic media. ***Journal of the Acoustical Society of America***, 77(3), 806-812.

Pei, Z. L., Fu, L.-Y., Sun W. J., Jiang, T., and Zhou, B. Z. (2012). Anisotropic finite-difference algorithm for modeling elastic wave propagation in fractured coalbeds. ***Geophysics***, 77(1), C13-C26.

Prioul, R., Bakulin, A., and Bakulin, V. (2004). Nonlinear rock model for estimation of 3D subsurface stress in anisotropic formation: theory and laboratory verification. ***Geophysics***, 62, 415–425.

Rasolofosaon, P. (1998). Stress–induced seismic anisotropic revisited. ***Revue de l'Institut Francais du Petrole,*** 53, 679–692.

Saenger, E. H. and Shapiro, S. A. (2002). Effective velocities in fractured media: a numerical study using the rotated staggered finite-difference grid. ***Geophysical Prospecting***, 50, 183-194.

Saenger, E. H., Gold, N., and Shapiro, S. A. (2000). Modeling the propagation of elastic waves using a modified finite-difference grid. ***Wave Motion***, 31, 77-92.

Sarkar, D., Bakulin, A., and Kranz, R. (2003). Anisotropic inversion of seismic data for stressed media: theory and a physical modeling study on Berea Sandstone. ***Geophysics***, 68, 690–704.

Sayers, C. M. (1988). Stress-induced ultrasonic wave velocity anisotropy in fractured rock. ***Ultrasonics***, 26, 311–317, doi: 10.1016/0041-624X(88) 90028-5.

Sayers, C. M. (2002). Stress-dependent elastic anisotropy of sandstones. ***Geophysical Prospecting***, 50, 85–95, doi: 10.1046/j.1365-2478.2002.00289.x.

Shapiro, S. A. (2003). Elastic piezosensitivity of porous and fractured rocks. ***Geophysics***, 68(2), 482-486.

Shapiro, S. A. (2017). Stress impact on elastic anisotropy of triclinic porous and fractured rocks. ***Journal of Geophysical Research: Solid Earth***, 122(3), 2034-2053.

Shapiro, S. A. and Kaselow, A. (2005). Porosity and elastic anisotropy of rocks under tectonic stress and pore-

pressure changes. ***Geophysics***, 70, N27–N38, doi:10.1190/1.2073884.

Shuck, E. L., Davis, T. L., and Benson, R. D. (1996). Multicomponent 3-D characterization of a coalbed methane reservoir. ***Geophysics***, 61, 315–330, doi: 10.1190/1.1443961.

Sinha, B. K. and Kostek, S. (1996). Stress-induced azimuthal anisotropy in borehole flexural waves, ***Geophysics***, 61, 1899–907.

Sinha, B. K. and Plona, T. J. (2001). Wave propagation in rocks with elastic-plastic deformations. ***Geophysics***, 66(3), 772-785.

Sripanich, Y., Vasconcelos, I., Tromp, J., and Trampert, J. (2021). Stress-dependent elasticity and wave propagation—New insights and connections. ***Geophysics***, *86*(4), W47-W64.

Thomsen, L. (1986). Weak elastic anisotropy. ***Geophysics***, 51, 1954–1966, doi: 10.1190/1.1442051.

Thurston, R. N. and Brugger, K. (1964). Third-order elastic constants and the velocity of small amplitude elastic waves in homogeneously stressed media. ***Physical Review***, 133(6A), A1604.

Trefethen, L. N., and Halpern, L. (1986). Well-posedness of one-way wave equations and absorbing boundary conditions. ***Math Comput***, 47(176), 421–435.

Tsvankin, I. (1997). Anisotropic parameters and P-wave velocity for orthorhombic media. ***Geophysics***, 62(4), 1292-1309.

Wang, W., and Schmitt, D. R. (2021). Static measurements of the third-order elastic constants of rocks. In ***ARMA US Rock Mechanics/Geomechanics Symposium*** (pp. ARMA-2021).

Walsh, J. B. (1965). The effect of cracks on the compressibility of rock. ***Journal of Geophysical Research: Solid Earth***, 70(2), 381–389, doi:10.1029/ JZ070i002p00381.

Wei, W. and Fu, L.-Y. (2014). Monte Carlo simulation of stress-associated scattering attenuation from laboratory ultrasonic measurements. ***Bull Seismol Soc Am***, 104, 931–943.

Wei, Y., Ba, J., and Carcione, J. M. (2022). Stress effects on wave velocities of rocks: Contribution of crack closure, squirt flow and acoustoelasticity. ***Journal of Geophysical Research: Solid Earth***, 127(10), e2022JB025253.

Winkler, K. W. and Liu, X. (1996). Measurements of third-order elastic constants in rocks. ***Journal of the Acoustical Society of America***, 100(3), 1392–1398.

Winkler, K. W. and McGowan, L. (2004). Nonlinear acoustoelastic constants of dry and saturated rocks. ***Journal of Geophysical Research: Solid Earth***, 109(B10), 67–85.

Wu, R. S. (1989). ***Seismic wave scattering***. In: James D, ed. Encyclopedia of Solid Earth Geophysics. New York: Van Nostrand Reinhold. 1166– 1187.

Yang, H., Fu, L.-Y., Fu, B. Y., and Müller, T. M. (2022a). Acoustoelastic FD simulation of elastic wave propagation in prestressed media. ***Frontiers in Earth Science***, doi: 10.3389/feart.2022.886920.

Yang, H., Fu, L.-Y., Fu, B. Y., and Du, Q. (2022b). Poro-acoustoelasticity FD simulation of elastic wave propagation in prestressed porous media. ***Geophysics***, 87(4), T329-T345.

Yang, H., Fu, L.-Y., Li, H., Du, Q., and Zheng, H. (2023). 3D acoustoelastic FD modeling of elastic wave propagation in prestressed solid media. ***Journal of Geophysics and Engineering***, 20(2), 297-311.

Zhang, Y., Fu, L.-Y., Zhang, L., Wei, W., and Guan, X. (2014). Finite difference modeling of ultrasonic propagation (coda waves) in digital porous cores with un-split convolutional PML and rotated staggered grid. ***J Appl Geophys***, 104, 75–89.

Zhao, L., Yao, Q., Han, D. H., Yan, F., and Nasser, M. (2015). Characterizing the effect of elastic interactions on the effective elastic properties of porous, cracked rocks. ***Geophysical Prospecting***, 64, 157–169, doi: 10 .1111/1365-2478.12243.

Zheng, H. C., Fu, L.-Y., Yang, H. D., Fu, B. Y., and Deng, W. B. (2024). Padé acoustoporoelasticity for 3D wave propagation in prestressed porous rocks with inelastic deformations. ***IEEE Transactions on Geoscience and Remote Sensing***, 61, 4503813, doi: 10.1109/TGRS.2024.3369173.

Zheng, Y. C., Fang, X. D.， Fehler, M. C. (2013). Seismic characterization of fractured reservoirs by focusing Gaussian beams. ***Geophysics***, 78(4), A23-A28.

Zhou, H., Jia, X. P., Fu, L.-Y., and Tourin, A. (2021) Monte-Carlo simulations of ultrasound scattering and absorption in finite-size heterogeneous materials. ***Physical Review Applied***, 16(3), 034009. DOI: 10.1103/PhysRevApplied.16.034009.

Zhou, H., Jia, X. P., Fu, L.-Y., and Tourin, A. (2023). Seismic wave scattering and dissipation in fractured shales. ***TechRxiv***, Preprint, DOI: 10.48550/arXiv.2301.00713.